This article has been accepted for publication in a future issue of this journal, but has not been fully edited. Content may change prior to final publication. Citation information: DOI 10.1109/TCI.2019.2922477, IEEE Transactions on Computational Imaging
TCI-00738-2018

Photon allocation strategy in region-of-interest tomographic imaging

Zheyuan Zhu[1], Hsin-Hisung Huang[2], and Shuo Pang[1]

***Abstract*— Photon counting detection is a promising approach towards dose reduction in x-ray computed tomography (CT). Full CT reconstruction from a fraction of the detected photons required by energy-integrating detectors has been demonstrated. In medical and industrial CT applications, projection truncation to the region-of-interest (ROI) is another effective way of dose reduction, as information from the ROI is usually sufficient for diagnostic purposes. Truncated projections pose an ill-conditioned inverse problem, which can be improved by including measurements from the exterior region. However, this trade-off between the interior reconstruction quality and the additional exterior measurement (extra dose) has not been studied. In this manuscript, we explore the number of detected x-ray photons as a new dimension for measurement engineering. Specifically, we design a flexible, photon-efficient measurement strategy for ROI reconstruction by incorporating the photon statistics at extremely low flux level (16 photons per pixel). The optimized photon-allocation strategy shows a 10 to 15-fold lower normalized mean square error (NMSE) in ROI than truncated projections, and a 2-fold lower NMSE in ROI than whole-volume CT scan. Our analysis in few-photon interior tomography could serve as a new framework for dose-efficient, task-specific x-ray image acquisition design.**

***Index Terms*— photon statistics, single-photon detection, computed tomography, interior tomography, dose reduction, computational imaging.**

I. Introduction

Due to the ionization nature of x-ray radiation, dose reduction is a critical design consideration in x-ray based imaging modality, especially in computed tomography (CT) where a series of projections are acquired during the acquisition process [1,2]. CT systems equipped with photon counting detectors (PCD) have demonstrated a ~30% dose reduction compared with the energy-integrating counterparts, while maintaining the same image contrast [3,4]. In addition, PCDs can effectively reduce the dark noise and discriminate the unwanted signal through energy gating [5,6]. However, in the filtered backprojection framework, photon-counting CT still collects hundreds to thousands of photons per pixel on average for a satisfactory reconstruction [7]. Image recovery from low-dose measurements necessitates the consideration of photon statistics in the reconstruction [8]. For photon counts on the order of 10^2~10^3, Poisson likelihood can model the detected photons and infer the attenuation map [9–11]. More recently, image reconstruction from an average ~10 photons per pixel based on the binomial likelihood [12] has been demonstrated in the visible regime. Extending few-photon imaging framework to CT modality could potentially minimize radiation damage to the object of interest.

In medical or industrial applications, the ultimate imaging task is often diagnosis or detection of a specific feature, rather than whole-volume reconstruction. Majority of the medical diagnostic scans require high image quality only in a small volume, while the projections outside this volume only provide structural or orientation information [13]. In industrial CT inspection, the whole-volume scan could expose radiation-sensitive components, such as processers, flash memory, to potential damage [9,14]. The image processing tasks, on the other hand, focus on classifying material compositions or quantifying the localized defects (e.g. air cavity, porosity, etc.) [15]. Task-specific image acquisition design can potentially shorten imaging time and reduce radiation damage to the region irrelevant to the diagnostic goal. This paper investigates the acquisition strategies from the perspective of photon statistics, when only a small localized region within the object is of interest.

The image acquisition process designed specifically for ROI reconstruction, termed interior tomography, distributes the radiation exclusively to the ROI, resulting in a series of truncated projections [16]. A unique and stable ROI solution is possible, provided that either a sub-region within the ROI is known [17,18], or the sample is piecewise constant [19,20]. However, the additional information of samples may not always be available [21,22]. Another solution is to use low-resolution projection from the exterior region to stabilize the ROI reconstruction [13,23]. This approach can be considered as a trade-off between reconstruction stability of whole CT scan and dose reduction benefit of truncated scan. Yet this trade-off has not been quantitatively studied, mainly because the illumination or integration time of each pencil beam is not easily adjustable in a conventional setup [24]. Recently, a time-stamp photon-counting X-ray imaging method has been developed [25]. Instead of counting the number of photons within a fixed integration time, the elapsed time is recorded when a pre-allocated photon count has been reached. With this photon-counting setup, we explore the photon allocation strategies for the ROI reconstruction, given a fixed total detected photon budget. Based on the statistics of the photon

This work was supported by National Science Foundation under Grant DMS-1615124.

1. Z. Zhu and S. Pang are with CREOL, The College of Optics and Photonics, University of Central Florida, Orlando, FL, 32816-2700 (e-mails: zyzhu@knights.ucf.edu, pang@creol.ucf.edu)

2. H.-H Huang is with Department of Statistics, University of Central Florida, Orlando, FL, 32816-2370 (e-mail: Hsin-Hsiung.Huang@ucf.edu)

This article has been accepted for publication in a future issue of this journal, but has not been fully edited. Content may change prior to final publication. Citation information: DOI 10.1109/TCI.2019.2922477, IEEE Transactions on Computational Imaging
TCI-00738-2018

arrival time, we formulate the tomography reconstruction as a Bayesian estimator. The optimal photon allocation strategy is identified by the smallest mean square error (MSE) within the ROI, for a given total photon budget. ROI reconstructions from an average of 16 photons per pencil beam have been established in both simulations and experiments. The optimized allocation strategy has demonstrated as much as a ~15-fold improvement in ROI MSE compared with truncated projection measurements, and ~2-fold compared with a uniform whole volume CT scan under the same total photon budget.

This paper is organized as follows: Section 2 describes the setup of our photon-counting CT system, and models the measurement and reconstruction process with a negative binomial distribution. Section 3 describes the details of the simulation and experiment setups used to explore the optimal photon allocation strategy. Section 4 presents the ROI reconstruction in phantom simulations, and applies the optimized photon allocation strategy to scan a real sample. Section 5 discusses the discrepancy between our analytical model and the numerical estimator, as well as the truncation artifacts in interior photon allocation strategy. Section 6 concludes the whole paper.

II. Theory

A. Imaging principle

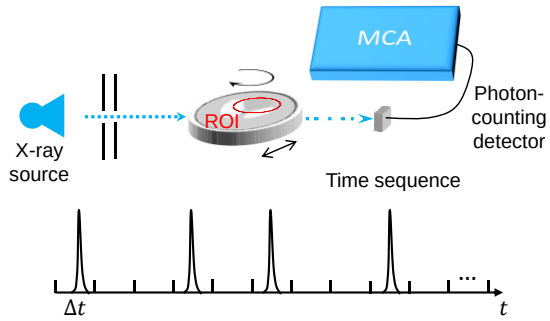

Fig. 1: Illustration of the photon-counting tomography scheme based on the time-stamp of each detected photon. The imaging task is to design an optimized photon allocation strategy among all the measurements to minimize the reconstruction error in ROI, marked by the red circle.

An x-ray tomography system with pencil-beam illumination and a single-pixel photon-counting detector has been constructed in our study. Fig. 1 illustrates the concept of the imaging setup. The incident x-ray beam is collimated by a pair of pinholes. To eliminate dark noise and obtain photon-limited signal, we specify a narrow bandwidth around the Kα line of the source for pulse censoring, so that photons whose energy fall outside the range are rejected. The source flux is well-controlled such that the probability λ of detecting one photon within one time interval is much smaller than 1 ($\lambda \sim 10^{-2}$), even when no sample is placed between the source and detector. The output signal is a series of discrete time intervals Δt, within which either one or no photon is registered.

Instead of directly counting the number of photons in a pre-defined integration time, we record the number of elapsed time intervals, $\mathbf{g}$, before the $\mathbf{r}$-th photon is detected for each pencil-beam measurement. To reconstruct the image of a 2D layer, the sample is translated across the pencil beam by s, which is the offset between the rotation center and the incident x-ray beam, and rotated around the vertical axis by angle ϕ.

Let $\mathbf{f} = \{f_{i_x,i_y}\} \in \mathbb{R}_+^{n_x \times n_y}$ denote the 2D attenuation map, where $(i_x, i_y) = \{1,2 \dots n_x\} \times \{1,2 \dots n_y\}$ is the pixel index of an $n_x \times n_y$ image. The discrete measurements $\mathbf{g}=\{g_{j_s,j_\phi}\} \in \mathbb{N}^{m_s \times m_\phi}$ and the photons received at each pencil beam $\mathbf{r} =\{r_{j_s,j_\phi}\} \in \mathbb{N}^{m_s \times m_\phi}$ are both indexed by $(j_s, j_\phi) = \{1,2 \dots m_s\} \times \{1,2 \dots m_\phi\}$, where m_s, m_ϕ represent the number of sampling in the translation s and rotation ϕ dimension, respectively. In our photon-counting framework, we assign a pre-defined photon number $\mathbf{r}$ to accumulate at each pencil beam, and measure the elapsed time intervals $\mathbf{g}$, which is a negative-binomial random variable. The reconstruction estimates the attenuation map $\hat{\mathbf{f}}$ from the observations of $\mathbf{g}$ with a set of known parameters $\mathbf{r}$. For a given parameter set $\{\mathbf{r}, \mathbf{f}\}$, the ROI reconstruction error is modeled by the weighted mean-square error of the estimator $\hat{\mathbf{f}}$, which is defined as

$$MSE_{\hat{\mathbf{f}}}(\mathbf{r}; \mathbf{f}) = \mathrm{E}_{\hat{\mathbf{f}}} \left\| \mathbf{w} \odot (\hat{\mathbf{f}} - \mathbf{f}) \right\|^2, \quad (1)$$

where $\mathbf{w} = \{w_{i_x,i_y} \in \{0,1\}, (i_x, i_y) = \{1,2, \dots, n_x\} \times \{1,2, \dots, n_y\}\}$ denotes the weight of each object pixel; w_{i_x,i_y}=0 for pixels outside the ROI, 1 for pixels inside the ROI; $\odot$ denotes the element-wise product between two vectors. The optimal photon allocation strategy looks for a photon map $\mathbf{r}$ that minimizes the ROI reconstruction MSE, given a fixed total detected photon budget

$$\sum_{j_s, j_\phi = 1}^{m_s, m_\phi} r_{j_s,j_\phi} = I_0. \quad (2)$$

In the following discussions involving linear indexing, the 2D map $\mathbf{f}$ and $\mathbf{w}$ are vectorized to $n = n_x \times n_y$ vectors $\mathbf{f} = \{f_i, i = 1,2 \dots, n\}$, $\mathbf{w} = \{w_i, i = 1,2 \dots, n\}$; $\mathbf{g}$ and $\mathbf{r}$ to $m = m_s \times m_\phi$ vectors $\mathbf{g} = \{g_j, j = 1,2, \dots, m\}$, $\mathbf{r} = \{r_j, j = 1,2, \dots, m\}$, respectively.

B. Negative binomial measurement model

Considering the sample attenuation, the probability of receiving one photon within one time interval Δt for the pencil-beam j is

$$T_j = \lambda \exp(-\sum_{i=1}^{n} A_{ji} f_i), \quad (3)$$

where $\mathbf{A} \in \mathbf{R}^{m \times n}, A_{ji} \geq 0$ is the CT transform matrix constructed from the distance-driven method [26]. The probability of receiving the r_j-th photon at g_j-th interval $(g_j, r_j \in N_+, g_j > r_j)$ for every pencil beam j follows a negative binomial distribution $(\sim NB(r_j, T_j))$ with explicit parameters $\mathbf{r} = (r_1, r_2, \dots r_m)$ and implicit parameters $\mathbf{f} =$

This article has been accepted for publication in a future issue of this journal, but has not been fully edited. Content may change prior to final publication. Citation information: DOI 10.1109/TCI.2019.2922477, IEEE Transactions on Computational Imaging
TCI-00738-2018

$(f_1, f_2, \dots f_n)$

$$p(\mathbf{g}|\mathbf{f};\mathbf{r}) = \prod_{j=1}^{m} \binom{g_j - 1}{r_j - 1} \left(1 - T_j\right)^{g_j - r_j} T_j{}^{r_j}. \tag{4}$$

Let $\pi(\mathbf{f})$ denote the prior distribution that describes the smoothness or sparsity constraints on the object. Since the attenuation map is non-negative $\mathbf{f} \geq 0$, we restrain the domain of $\pi(\mathbf{f})$ to non-negative values $\mathbf{f} \in \mathbb{R}_+^n$. The negative log-posterior distribution $L(\mathbf{f}|\mathbf{g};\mathbf{r})$ of waiting $\mathbf{g}$ intervals for $\mathbf{r}$ photons given the sample prior $\pi(\mathbf{f})$ is

$$\begin{aligned} L(\mathbf{f}|\mathbf{g};\mathbf{r}) &= -\log\left[\frac{p(\mathbf{g}|\mathbf{f};\mathbf{r})\pi(\mathbf{f})}{p(\mathbf{g};\mathbf{r})}\right] \\ &= -\sum_{j=1}^{m}\Bigg\{\log\binom{g_j - 1}{r_j - 1} \\ &\quad + \left(g_j - r_j\right)\log\left[1 - \lambda\exp\left(-\sum_{i=1}^{n} A_{ji} f_i\right)\right] \\ &\quad - r_j \sum_{i=1}^{n} A_{ji} f_i\Bigg\} + u(\mathbf{f}) + \log p(\mathbf{g};\mathbf{r}), \end{aligned} \tag{5}$$

where we introduce $u(\mathbf{f}) = -\log\pi(\mathbf{f})$ as the negative log-prior, $l(\mathbf{f}|\mathbf{g};\mathbf{r}) = \log p(\mathbf{g}|\mathbf{f};\mathbf{r})$ as the log-likelihood of the model parameter $\mathbf{f}$ in the negative binomial distribution, for simplicity. The object $\mathbf{f}$ is reconstructed by the maximum-a-posteriori (MAP) estimation, which minimizes the negative log-posterior distribution. The marginal distribution of the measurement $\log p(\mathbf{g};\mathbf{r})$ is independent of $\mathbf{f}$, and thus not included in the optimization.

$$\hat{\mathbf{f}}(\mathbf{g};\mathbf{r}) = \underset{\mathbf{f}'}{\operatorname{argmin}}\{-l(\mathbf{f}'|\mathbf{g};\mathbf{r}) + u(\mathbf{f}')\}. \tag{6}$$

C. Property of the measurement and estimator

In this section, we introduce some quadratic approximations that are essential to analyzing the behavior of the numerical MAP estimator (Eq. (6)), for a given object and photon counts $\{\mathbf{r}, \mathbf{f}\}$, and the prior distribution $\pi(\mathbf{f})$. To facilitate the discussion of the measurement distribution, given the parameter set $\{\mathbf{r}, \mathbf{f}\}$, we introduce auxiliary variables

$$\mathbf{t} = \left\{t_j(\mathbf{f}) = \log\frac{\lambda}{T_j(\mathbf{f})} = \sum_{i=1}^{n} A_{ji} f_i\,, j = 1,2,\dots,m\right\}, \tag{7}$$

which can be interpreted as the CT line-integrals. By setting the derivative of the negative binomial measurement (Eq. (4)) with respect to T_j to 0, and applying the invariance principle, the maximum likelihood (ML) estimation for t_j is achieved at

$$\hat{t}_j = \log\frac{\lambda r_j}{g_j}. \tag{8}$$

We then change the variable in the negative binomial distribution (Eq. (4)) from $\mathbf{g}$ to $\hat{\mathbf{t}}$ to derive the conditional distribution of $\hat{\mathbf{t}}$, $q(\hat{\mathbf{t}}|\mathbf{t}(\mathbf{f});\mathbf{r})$. The logarithm of $q(\hat{\mathbf{t}}|\mathbf{t};\mathbf{r})$ is

$$\begin{aligned} q(\hat{\mathbf{t}}|\mathbf{t};\mathbf{r}) &= \sum_{j=1}^{m} q_j(\hat{t}_j|t_j;r_j) \\ &= \sum_{j=1}^{m}\Bigg\{\log\frac{\Gamma(r_j\exp\hat{t}_j/\lambda)}{\Gamma(r_j\exp\hat{t}_j/\lambda - r_j + 1)\Gamma(r_j)} \\ &\quad + \left(\frac{r_j\exp\hat{t}_j}{\lambda} - r_j\right)\log\left[1 - \lambda\,exp(-t_j)\right] \\ &\quad + r_j\log(\lambda\exp(-t_j)) + \log(r_j\exp\hat{t}_j/\lambda)\Bigg\}, \end{aligned} \tag{9}$$

where $\sum_{i=1}^{n} A_{ji} f_i$ is replaced with t_j , g_j with $r_j \exp\hat{t}_j / \lambda$; and binomial coefficients in $p(\mathbf{g}|\mathbf{f};\mathbf{r})$ are expressed by the gamma functions. The additional term $\log(r\exp\hat{t}/\lambda)$ normalizes the distribution with respect to $\hat{\mathbf{t}}$. Based on Eq. (9), we introduce a couple of first-order approximations to the log-likelihood function to simplify the discussion of the distribution of $\hat{t}_j$. Since $\lambda{\sim}10^{-2}$, we take the first-order approximation for $\log(1 - \lambda\exp(-t_j)) \approx -\lambda\exp(-t_j)$, and according to Stirling's formula,

$$\frac{\Gamma\left(\frac{r_j\exp\hat{t}_j}{\lambda}\right)}{\Gamma\left(\frac{r_j\exp\hat{t}_j}{\lambda} - r_j + 1\right)} \approx \left(\frac{r_j\exp\hat{t}_j}{\lambda}\right)^{(r_j - 1)},$$

Eq. (9) is simplified to:

$$\begin{aligned} q(\hat{\mathbf{t}}|\mathbf{t};\mathbf{r}) &= \sum_{j=1}^{m}\big[r_j(\hat{t}_j - t_j) - r_j\exp(\hat{t}_j - t_j) \\ &\quad + r_j\lambda\exp(-t_j) + r_j\log r_j - \log\Gamma(r_j)\big]. \end{aligned} \tag{10}$$

Eq. (10) shows that the distribution of $\hat{t}_j$ is asymmetrically centered at $\hat{t}_j = t_j$. Taylor expansion on $q_j(\hat{t}_j|t_j;r_j)$ to the second order around $\hat{t}_j = t_j$ gives

$$\begin{aligned} q_j(\hat{t}_j|t_j;r_j) &= q_j(t_j) + q_j'(t_j)(\hat{t}_j - t_j) \\ &\quad + \frac{q_j''(t_j)(\hat{t}_j - t_j)^2}{2} + R(\hat{t}_j) \\ &= r_j\lambda\exp(-t_j) + r_j\log r_j - \log\Gamma(r_j) \\ &\quad + \frac{r_j(\hat{t}_j - t_j)^2}{2} + R(\hat{t}_j). \end{aligned} \tag{11}$$

The quadratic component in Eq. (11) implies that each random variable $\hat{t}_j$ approximately follows a normal distribution $N(\mu_{\hat{t}_j}, \sigma_{\hat{t}_j}^2)$ with mean $\mu_{\hat{t}_j}$ equal to the ground truth of CT line integral t_j, and a variance $\sigma_{\hat{t}_j}^2 = 1/r_j$ that depends only on the photon count. $R(\hat{t}_j)$ contains the higher-order Taylor expansion terms that introduce a negative skew to this normal distribution. When the photon number r_j reaches 16 and above, however, the skew becomes insignificant, which is discussed in Section V.A in detail.

Next, we discuss the property of the MAP estimator under a prior distribution $\pi(\mathbf{f})$. Here, we omit the non-negativity constraint, and consider the Gaussian family of distributions for obtaining closed-form solutions to the optimization

This article has been accepted for publication in a future issue of this journal, but has not been fully edited. Content may change prior to final publication. Citation information: DOI 10.1109/TCI.2019.2922477, IEEE Transactions on Computational Imaging

problem in Eq. (6)

$$\pi(\mathbf{f}) = \frac{\sqrt{\tau \det(\mathbf{D}\mathbf{D}^T)/2}}{\sqrt{(2\pi)^n}} \exp(-\tau\|\mathbf{D}\mathbf{f}\|^2) \tag{12}$$

where the regularization matrix $\mathbf{D} \in \mathbb{R}^{q\times n}$ projects the attenuation map $\mathbf{f}$ onto a q-dimensional sparse domain; the parameter τ controls the variance of the Gaussian prior. If $\mathbf{D}$ is the identity matrix $\mathbf{I}_n$, $\pi(\mathbf{f})$ becomes the L2-prior that punishes large values in $\mathbf{f}$. Notice that the widely-used total-variation (TV) regularization cannot be expressed as Gaussian prior due to its semi-norm definition. After a set of measurements, $\mathbf{g}$, are recorded with photon counts $\mathbf{r}$, we rewrite the likelihood of the parameter $\mathbf{f}$ in terms of the CT line-integral, $\mathbf{t}$, given $\{\mathbf{g}, \mathbf{r}\}$

$$\begin{aligned} l(\mathbf{f}|\mathbf{g};\mathbf{r}) &= \sum_{j=1}^{m} y_j(t_j) \\ &= \sum_{j=1}^{m} \left\{ \log \binom{g_j - 1}{r_j - 1} \right. \\ &\quad \left. + (g_j - r_j)\log\left[1 - \lambda \exp(-t_j)\right] - r_j t_j \right\}. \end{aligned} \tag{13}$$

Applying second-order Taylor-expansion to $y_j(t_j)$ around the estimated line-integral $\hat{t}_j = \log(\lambda g_j / r_j)$ yields [27]

$$\begin{aligned} y_j(t_j) &\approx y_j(\hat{t}_j) + y_j'(\hat{t}_j)(t_j - \hat{t}_j) + \frac{y_j''(\hat{t}_j)(t_j - \hat{t}_j)^2}{2} \\ &= \left\{ \log \binom{g_j - 1}{r_j - 1} + (g_j - r_j)\log\left[1 - \lambda \exp(-\hat{t}_j)\right] \right. \\ &\quad \left. - r_j \hat{t}_j \right\} - \frac{r_j (t_j - \hat{t}_j)^2}{2\left(1 - \frac{r_j}{g_j}\right)}, \end{aligned} \tag{14}$$

where the first-order derivative $y_j'(\hat{t}_j)$=0 for all $j = 1,2,\dots,m$; $r_j/g_j \approx \lambda \exp\sum_{i=1}^{n} A_{ij} f_i \ll 1$ is negligible on the denominator. The Taylor-expansion in Eq. (14) reduces the MAP estimator in Eq. (6) to a least-square problem weighted on photon count $\mathbf{r}$

$$\begin{aligned} \hat{\mathbf{f}}(\hat{\mathbf{t}};\mathbf{r}) &= \underset{\mathbf{f}'}{\operatorname{argmin}} \{ -\sum_{j=1}^{m} y_j(t_j(\mathbf{f}')) + \tau\|\mathbf{D}\mathbf{f}'\|_2^2 \} \\ &\approx \underset{\mathbf{f}'}{\operatorname{argmin}} \{ \frac{1}{2} \left\| diag(\sqrt{\mathbf{r}})(\mathbf{A}\mathbf{f}' - \hat{\mathbf{t}}) \right\|_2^2 + \tau\|\mathbf{D}\mathbf{f}'\|_2^2 \}, \end{aligned} \tag{15}$$

where the zero-order terms in y_j are independent of $\mathbf{f}$, and can thus be neglected in the optimization; $diag(\sqrt{\mathbf{r}})$ denotes the diagonal matrix constructed from the vector $\sqrt{\mathbf{r}}$. The resulting objective function in Eq. (15) $\varepsilon(\mathbf{f}) = \frac{1}{2}\left\| diag(\sqrt{\mathbf{r}})(\mathbf{A}\mathbf{f} - \hat{\mathbf{t}}) \right\|_2^2 + \tau\|\mathbf{D}\mathbf{f}\|_2^2$ has a gradient

$$\nabla\varepsilon(\mathbf{f}) = \mathbf{A}^T diag(\mathbf{r})(\mathbf{A}\mathbf{f} - \hat{\mathbf{t}}) + 2\tau\mathbf{D}^T\mathbf{D}\mathbf{f} \tag{16}$$

and Hessian matrix

$$\mathbf{H}\left(\varepsilon(\mathbf{f})\right) = \mathbf{A}^T diag(\mathbf{r})\mathbf{A} + 2\tau\mathbf{D}^T\mathbf{D}. \tag{17}$$

For a properly-chosen regularization matrix $\mathbf{D}$, $\mathbf{H}$ is positive-definite and can thus be conceived as the inverse covariance of the posterior distribution $p(\mathbf{f}|\,\hat{\mathbf{t}})$. Eq. (15) has an explicit solution similar to a Tikhonov regularization [28] weighted on $\mathbf{r}$

$$\hat{\mathbf{f}}(\hat{\mathbf{t}};\mathbf{r}) = \mathbf{H}^{-1}(\mathbf{r})\mathbf{A}^T diag(\mathbf{r})\hat{\mathbf{t}}. \tag{18}$$

where $\mathbf{H}^{-1}(\mathbf{r})$ denotes the inverse of Hessian matrix $\mathbf{H}(\mathbf{r})$. Since the estimator $\hat{\mathbf{f}}$ is a linear superposition of Gaussian variables $\hat{\mathbf{t}}$, the distribution of $\hat{\mathbf{f}}$ thus follows a multivariate Gaussian distribution with mean

$$\boldsymbol{\mu}_{\hat{\mathbf{f}}}(\mathbf{r};\mathbf{f}) = \mathbf{H}^{-1}(\mathbf{r})\mathbf{A}^T diag(\mathbf{r})\mathbf{A}\mathbf{f} \tag{19}$$

and covariance

$$\boldsymbol{\Sigma}_{\hat{\mathbf{f}}}(\mathbf{r}) = \mathbf{H}^{-1}(\mathbf{r})\mathbf{A}^T diag(\mathbf{r})\mathbf{A}\mathbf{H}^{-1}(\mathbf{r}). \tag{20}$$

The MSE of the estimator consists of the bias square and the variance of the pixels within ROI

$$\begin{aligned} MSE_{\hat{\boldsymbol{f}}}(\boldsymbol{r};\boldsymbol{f}) &= \left\| \left(\boldsymbol{\mu}_{\hat{\boldsymbol{f}}}(\boldsymbol{r};\boldsymbol{f}) - \boldsymbol{f}\right)\boldsymbol{w} \right\|^2 + \\ &\quad tr\left[diag(\boldsymbol{w})\boldsymbol{\Sigma}_{\hat{\boldsymbol{f}}}(\boldsymbol{r}) \right]. \end{aligned} \tag{21}$$

Eq. (19) indicates that without regularization, τ=0, the estimator (Eq. (18)) is unbiased. When $\tau \neq 0$, the Gaussian prior introduces a bias to the estimator and reduces its variance. The tradeoff between bias and variance implies the existence of a best regularization parameter, τ, that yields minimum MSE in the reconstruction.

III. Materials and Methods

A. Phantoms and photon maps

Two simulation phantoms were used to evaluate the performance of the estimator (Eq. (6)) with different photon allocation strategies. Simulation phantom 1 was a real abdomen CT slice (Subject ID 116-HM10395) [29]. The raw image underwent 2 X 2 binning to reduce the number of pixels to 256 X 256, with a pixel size of 2mm X 2mm after binning. The region around the cross-section of the vertebra was selected as the ROI, which was centered at 80mm (40 pixels) away from the rotation center, and was 80mm in diameter. Phantom 2 was a 256 X 256 Shepp-Logan phantom with a pixel size of 1mm. The 15mm-diameter region (15-pixel wide) was defined as the ROI, which was 4mm (4 pixels) away from the rotation center. For both phantoms, the translation step of the pencil beam matched the spatial grid of the phantom (2mm for abdomen slice, 1mm for Shepp-Logan phantom). The projections were sampled at 0.5° interval, which matches the Nyquist sampling in the reciprocal space.

The photon allocation strategy in the ROI and exterior region is modeled by assigning different number of photon counts $\mathbf{r}$ to accumulate at each measurement j. To avoid enumerating all the possibilities of $\mathbf{r}$ that satisfy the total photon budget constraint, we confine our choice of the 2D photon allocation map to a trapezoid function:

This article has been accepted for publication in a future issue of this journal, but has not been fully edited. Content may change prior to final publication. Citation information: DOI 10.1109/TCI.2019.2922477, IEEE Transactions on Computational Imaging

$$r_{j_s,j_\phi} = \frac{I_0(1-\beta)}{m_\phi} + \begin{cases} \frac{1}{m_\phi}\frac{I_0\beta\delta x}{2\sigma+\Delta}, & |j_s\delta x - s_c| \le \sigma \\ \frac{1}{m_\phi}\frac{I_0\beta\delta x}{2\sigma+\Delta}\frac{\sigma+\Delta-|j_s\delta x - s_c|}{\Delta}, & \sigma < |j_s\delta x - s_c| < (\sigma+\Delta) \\ 0, & |j_s\delta x - s_c| \ge (\sigma+\Delta) \end{cases} \quad (22)$$

$$j_s = 1,2,\ldots,m_s$$
$$j_\phi = 1,2,\ldots,m_\phi$$

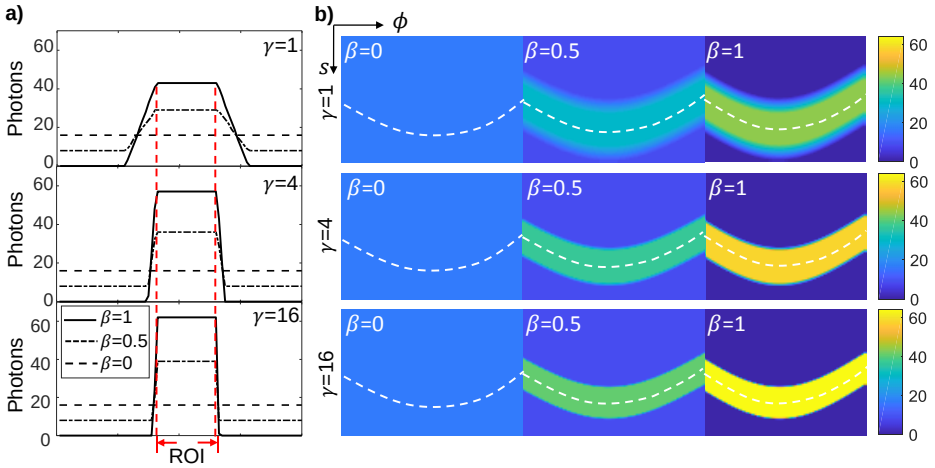

Fig. 2: Photon distribution profiles used in the simulation. (a) Photon allocation profiles at γ=1, 4 and 16 under 0° projection. (b) two-dimensional photon allocation maps for β=0, 0.5 and 1, γ=1, 4 and 16.

where δx is the translation step size; σ is the radius of ROI; β controls the interior/exterior ratio; Δ denotes the width of the transition region where the photon number drops from maximum to the minimum; when Δ=0, the photon allocation profile becomes a rectangular shape. In our simulation, we define $\gamma = \sigma/\Delta$ as the shape parameter that describes the slope of the photon allocation profile across the ROI boundary. s_c is the center coordinate of ROI at different projections, and is calculated via

$$s_c = s_{offset}\sin(\phi + \phi_{offset}) \quad (23)$$

where s_{offset} is the offset between the ROI center and the rotation center; ϕ_{offset} is the azimuthal coordinate of the ROI center with respect to the rotation center. Fig. 2 (a) plots the photon allocation profile along the translation direction, s, with γ=1, 4 and 16 under 0° projection. For phantom 1, the two-dimensional photon allocation maps for β=0, 0.5 and 1 are shown in Fig. 2 (b). The white, dashed curves mark the trajectory of ROI center as the sample undergoes 180° rotation. The reconstruction quality is assessed with the mean square error (MSE). We normalize the MSE according to the L2-norm of the ROI to obtain normalized MSE (NMSE), which makes the scale consistent among different samples and ROIs.

$$NMSE = \left\|\boldsymbol{w}^T(\hat{\boldsymbol{f}} - \boldsymbol{f})\right\|^2 / \|\boldsymbol{w}^T\boldsymbol{f}\|^2 \quad (24)$$

Our simulation goal was to find the best photon allocation strategy, expressed by the two parameters (β,γ), that minimizes the NMSE between the reconstruction and the object within ROI.

B. Simulation setup

The 2D photon map **r** was calculated from Eq. (22) and rounded to the nearest integer. Each simulated measurement summed up r_j geometric random numbers $Geo(T_j)$ (generated by MATLAB R2017B) to represent the number of time intervals g_j before the arrival of the r_j-th photon, where T_j is calculated from the CT line integral $T_j = \lambda[\mathbf{Af}]_j$. In case zero photons were assigned to a particular pencil beam, the corresponding row in CT matrix **A** that represented this measurement was removed. In total, 12 interior/exterior ratios β (from 0 to 1 at 0.1 step, and 0.95) and 3 shape parameters γ=1, 4, and 16 were combined as different photon allocation strategies in our simulations. For each photon map **r**, we ran 15 instances of simulated measurements **g** and reconstructions $\hat{\mathbf{f}}$. Based on the 15 reconstruction instances $\hat{\mathbf{f}}$, we calculated the NMSE within the ROI, and plotted its average and standard deviation. We also recorded the pixel-wise mean, variance and MSE map for comparison with our analytical approximation.

C. Experiment setup

The experimental photon-counting system was implemented by connecting the electrically censored pulses from the Si-PIN detector (X-123, AMPTEK) to a data acquisition device

This article has been accepted for publication in a future issue of this journal, but has not been fully edited. Content may change prior to final publication. Citation information: DOI 10.1109/TCI.2019.2922477, IEEE Transactions on Computational Imaging

(USB6353, National Instrument) operating in the edge-counting mode. The detector system was configured to run at a counting interval of Δt=10μs. The X-ray source was a copper-anode tube (XRT60, Proto Manufacturing) operating at 12kV. The current of the tube had been reduced to 1mA to minimize the probability of registering two photons in the same time interval. The incident X-ray beam was collimated by a pair of 0.5mm pinholes located at 20cm away from the X-ray focus. With this setup geometry, the probability of detecting one photon within one Δt time interval from the collimated beam was λ=0.015. The sample was mounted on a rotational stage (RV120PP, Newport) and a linear stage (UTM150CC, Newport) for pencil-beam CT scan.

An acrylic resolution target was scanned in our experiments. The target was laser-machined with 0.5-1.0mm line-width groups. The 0.6mm group was defined as the ROI. The sample was translated at a step size of 0.2mm for 81 steps, and rotated by 2° step size to cover 180° projections. For each pencil-beam measurement, we collected the entire 1s time stamps and used all the detected photons to form a reference image. The few-photon measurement had a detected photon budget of 16 photons per pencil beam on average. We extracted the first r_j photons from the 1s time stamp according to our optimized strategy for reconstruction.

D. Reconstruction algorithm

The optimization problem in Eq. (6) is solved numerically with a modified SPIRAL-TAP[30], which is a gradient-descent algorithm combined with regularization in each iteration. The gradient and Hessian of our negative binomial log-likelihood are respectively

$$\nabla l(\mathbf{f}) = \mathbf{A}^T\left(\mathbf{r} - \frac{\lambda(\mathbf{g}-\mathbf{r})\odot\exp(-\mathbf{Af})}{1-\lambda\exp(-\mathbf{Af})}\right), \tag{25}$$

$$\mathbf{H}\big(l(\mathbf{f})\big) = \mathbf{A}^T\left(\frac{\lambda(\mathbf{g}-\mathbf{r})\odot\exp(-\mathbf{Af})}{(1-\lambda\exp(-\mathbf{Af}))^2}\right)\mathbf{A}. \tag{26}$$

Because the probability λ of detecting one photon within each time interval is on the order of 10^{-2}, it is very rare ($<10^{-4}$) to detect multiple photons in one time interval. As a result, $g_j - r_j$ has a high probability of being non-negative, which suggests that the Hessian has a high probability of being positive semidefinite for non-negative object $\mathbf{f} \geq \mathbf{0}$. The step parameter α_k, which is the inverse of step size at k-th iteration, is chosen according to the modified Barzilai-Borwein method described in Ref. [30]. Notice that Eq. (26) contains a singular point on the denominator. To avoid moving the solution across this singular point, we enforce a minimum value, α_{min}, in each iteration if the chosen α value is smaller than α_{min}. The iteration stops when the relative change in $L(\mathbf{f})$ is smaller than 10^{-6}.

The modified SPIRAL was initialized with a trial solution $\mathbf{f}^{(0)} = \mathbf{A}^T \log\lambda\mathbf{r}/\mathbf{g}$. The change in the solution $\delta\mathbf{f}$ was chosen as $\delta\mathbf{f} = \mathbf{f}^{(0)}$ in the first iteration, and $\delta\mathbf{f} = \mathbf{f}^{(k)} - \mathbf{f}^{(k-1)}$ in subsequent iterations $k \geq 2$. The major computational burden was the calculation of matrix-vector product $\mathbf{Af}$, $\mathbf{A^Tr}$ or $\mathbf{A^Tg}$, which all had a complexity of $O(mn)$. We pre-calculated the vector $\mathbf{Af}$ and $\mathbf{A}\delta\mathbf{f}$ at the beginning of each iteration for use in both gradient and Hessian. This resulted in three $O(mn)$ operations in each iteration.

The regularization step in our modified SPIRAL-TAP was implemented with either TV or L2-norm constraint. The TV regularization penalizes the L2-norm of the total-variation

$$u(\mathbf{f}) = \tau\sum_{i_x=1}^{n_x}\sum_{i_y=1}^{n_y}\sqrt{(f_{i_y+1,\,i_x} - f_{i_y,\,i_x})^2 + (f_{i_y,\,i_x+1} - f_{i_y,\,i_x})^2} \tag{27}$$

and enforces non-negativity with the FISTA algorithm [31]. The L2-norm constraint belongs to a special case in the Gaussian prior family, with $\mathbf{D}$ being the identity matrix $\mathbf{I}_n$ in Eq. (12). This leads to the solution to the regularization step at k-th iteration

$$\mathbf{f}^{k+1} = \{\max\left(0, \frac{f_i^{k+1,temp}}{1+\tau/\alpha^k}\right), i = 1,2,\dots,n\} \tag{28}$$

where $1/\alpha^k$ is the step size along the gradient; $\mathbf{f}^{k+1,temp}$ is the intermediate result after the k-th gradient-descent step; and $\mathbf{f}^{k+1}$ is the final result after regularization. The negative values in $\mathbf{f}^{k+1,temp}$ are replaced with 0 to enforce non-negativity. For both constraints, the regularization strength, τ, ranging from 10^1 to 10^3 at $10^{0.5}$ step, was optimized for minimum NMSE in the reconstruction.

IV. Numerical and Experimental Results

A. Phantom simulations with L2-norm constraint

1) The effect of γ on NMSE

We first evaluated the ROI reconstruction performances with different photon allocation strategies using the abdomen phantom. The regularization parameter that yielded minimal NMSE for each photon map was selected. The total detected photon budget was 1.5×10^6, corresponding to 16 photon counts per pencil beam on average. Fig. 3 plots the reconstruction NMSE within the ROI in terms of interior/exterior ratio β and shape parameter γ. As β increases from 0 up to 0.9, more photons are allocated to the ROI, therefore decreasing its reconstruction NMSE. This simulation trend was also reflected by the analytical MSE from our approximation (Eq. (21)). The optimal β and the minimum NMSE are summarized in Table 1 for γ=1, 4 and 16. The best photon strategy is β=0.9, γ=4 in the numerical simulation. It is worth noting that for β<0.9, the NMSE of γ=1 is generally higher than γ=4 and 16. This is because for the same β, γ=1 allocates more photons in the vicinity outside the ROI boundary, which reduces the ROI photon counts as a result of the fixed total photon budget. Therefore a shape parameter γ>1 is generally preferred.

TABLE 1:
THE OPTIMAL βS AND NMSES FOR DIFFERENT SHAPE PARAMETER γ

Shape parameter $\boldsymbol{\gamma}$	$\boldsymbol{\gamma}$=1	$\boldsymbol{\gamma}$=4	$\boldsymbol{\gamma}$=16
Optimal β	1	0.9	0.8
NMSE	0.81±0.02%	0.75±0.02%	0.79±0.03%

This article has been accepted for publication in a future issue of this journal, but has not been fully edited. Content may change prior to final publication. Citation information: DOI 10.1109/TCI.2019.2922477, IEEE Transactions on Computational Imaging
TCI-00738-2018

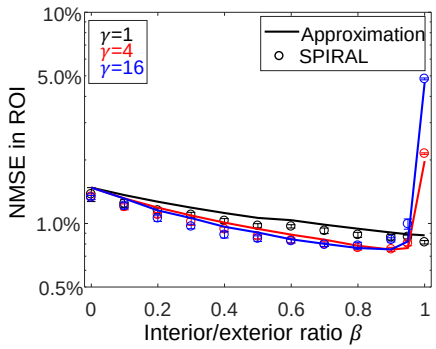

Fig. 3: Simulated and predicted ROI reconstruction NMSE vs. the interior/exterior ratio β for γ=1, 4, and 16.

Fig. 4 exemplifies the reconstruction instances at different (β,γ) combinations. The ground truth and ROI of the abdomen phantom are shown in Fig. 4 (a) for comparison. Fig. 4 (b-d) show the reconstruction at β=0, the optimized β in the simulation, and β=1. At high β values, the absence of the projection measurement creates artifacts on the boundary between measured and unmeasured regions (Fig. 4 (c3-d3)), which are consistent with the truncation artifacts associated with the non-localized filtered back-projection (FBP) kernel [16,32]. The photon allocation strategy β=1, γ=16 is equivalent to the projection truncation in interior tomography. Notice that for γ=1, the measured region extends to twice the ROI size. As a result, the truncation artifact is not visible within the display window of Fig. 4 (b3) and the NMSE does not increase for β=1. Our simulation and analytical approximates suggest that the optimal strategy is to deposit 10%~20% of the total photon budget outside ROI, which reduces the NMSE in ROI by 6 times compared to concentrating all available photon budgets in the ROI (β=1, γ=16).

2) The effect of ROI size on NMSE

As β increases from 0 to the optimal value, the general trend of NMSE for different γs is to decrease, then increase dramatically as β passes the optimal value and missing measurements start to appear. In the following discussions, we focus on the case of γ=16, which incorporates the conventional interior tomography strategy. Fig. 5 plots the NMSE vs. β with different ROI diameters 2σ, normalized with respect to the total phantom size. For this simulation, we scaled up/down the total photon budget I_0 so that for the same β, the average number of photons per beam dedicated to the ROI $I_0\beta/(2\sigma m_s)$ remained unchanged regardless of the ROI size. All the ROIs in this simulation are centered on the same location as in Fig. 4 (a). Fig. 6 shows the reconstruction instances for β=0, optimized β, and β=1 when ROI diameter equals 10%, 15%, 20% and 25% of the full phantom dimension, respectively. The optimal β and NMSE are summarized in Table 2. These results indicate that the optimized β parameter is generally determined by the portion of ROI within the whole sample. A smaller ROI requires a lower β for optimal reconstruction performance.

TABLE 2:
THE OPTIMAL β AND NMSES FOR DIFFERENT ROI SIZES

ROI size ratio	10%	15%	20%	25%
Optimal β	0.8	0.8	0.9	0.95
NMSE	0.63% ±0.02%	0.78% ±0.03%	0.72% ±0.01%	0.71% ±0.02%

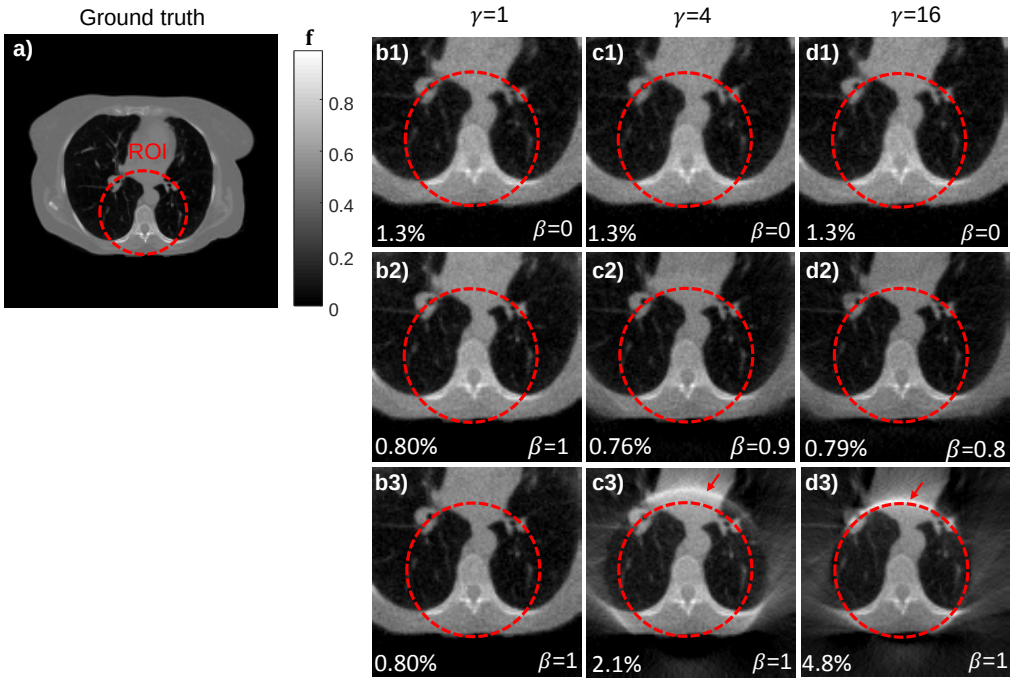

Fig. 4: (a) Ground truth of the abdomen phantom used in the simulation. (b-d) Reconstruction of the abdomen phantom with different shape parameters γ for (b) β=0 (uniform), (c) optimal β, and (d) β=1. The ROI is marked by the red circle. The red arrows highlight the truncation artifacts. The numbers in the left bottom of each reconstruction indicate the NMSE within ROI. The display window is 200mm X 200mm.

This article has been accepted for publication in a future issue of this journal, but has not been fully edited. Content may change prior to final publication. Citation information: DOI 10.1109/TCI.2019.2922477, IEEE Transactions on Computational Imaging

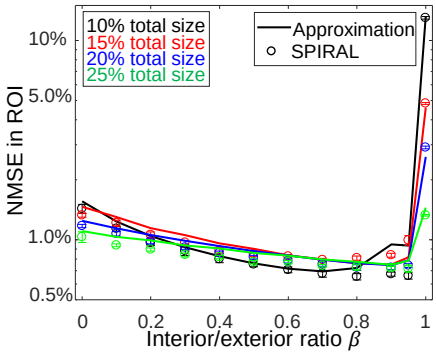

Fig. 5: ROI reconstruction NMSE vs. the interior/exterior ratio β for ROI diameters equal to 10%, 15%, 20% and 25% of the phantom size, with γ=16.

3) The effect of total photon budget on NMSE

Next, we focus on the allocation strategies for different total photon budgets, ranging from an average of 16 photons per beam to 1024 photons perbeam. Fig. 7 plots the NMSE as a function of β with γ=16 at different photon budgets for the ROI shown in Fig. 4 (a). Fig. 8 shows the phantom reconstruction instances with respect to different photon budgets and β. The NMSE of uniform, interior and optimized photon allocations are summarized in Table 3. The ROI reconstruction NMSEs for all three strategies decrease as the average number of photons per beam increases, which displays a trade-off between reconstruction quality and photon budget. The results indicate that the optimal photon-allocation strategy consistently outperforms the full-scan (β=0) by 1.5~3-fold, and interior-scan (β=1) strategies by ~10-fold, in the trade space between NMSE and photon budget.

TABLE 3:
THE OPTIMAL βS FOR UNIFORM, OPTIMIZED AND INTERIOR PHOTON ALLOCATION STRATEGIES WITH DIFFERENT TOTAL PHOTON BUDGETS

Average photons per beam	16	64	256	1024
Optimal β	0.8	0.8	0.8	0.8
Uniform strategy NMSE	1.3% ±0.04%	0.56% ±0.04%	0.31% ±0.04%	0.28% ±0.01%
Optimal strategy NMSE	0.79% ±0.02%	0.29% ±0.01%	0.12% ±0.002%	0.074% ±0.003%
Interior strategy NMSE	4.8% ±0.05%	4.2% ±0.01%	4.0% ±0.03%	3.9% ±0.01%

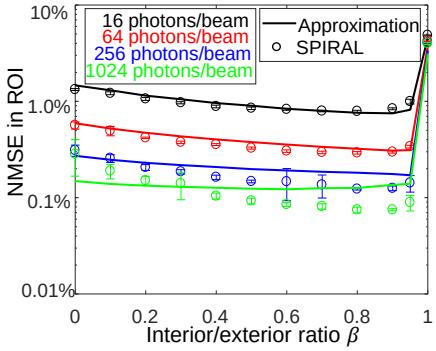

Fig. 7: ROI reconstruction NMSE vs. the interior/exterior ratio β at different total photon budget, with γ=16. The black, red, blue and green curves represent 16, 64, 256 and 1024 detected photons per beam on average.

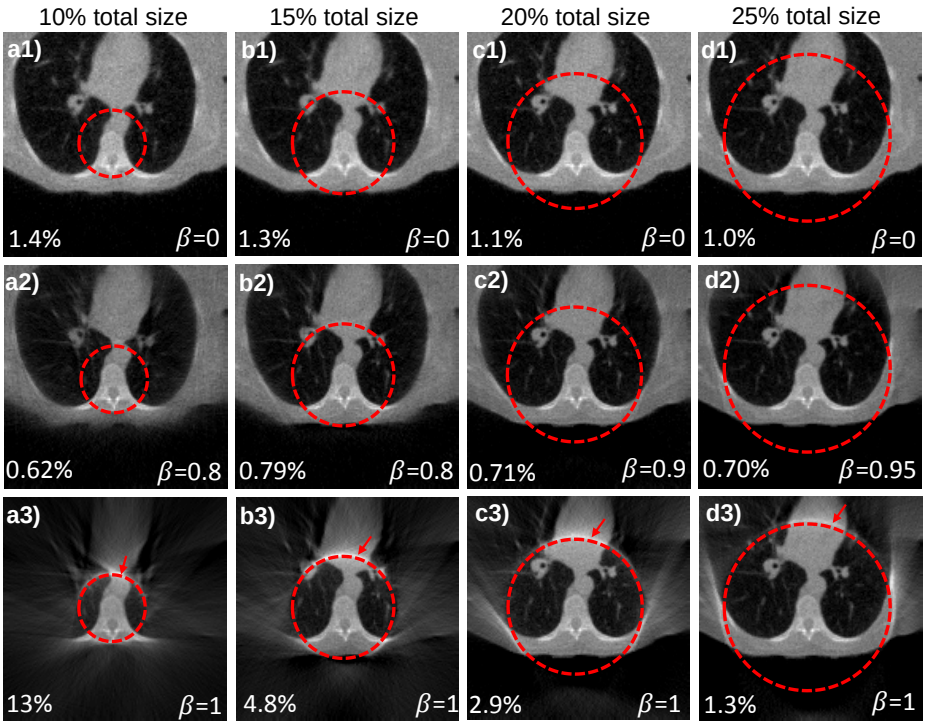

Fig. 6: Reconstruction of the abdomen phantom with ROI sizes equal to (a) 10% (b) 15% (c) 20% (d) 25% of the total size, for (1) β=0 (uniform), (2) optimal β, and (3) β=1, with γ=16. The ROI is marked by the red circle. The red arrows highlight the truncation artifacts. The numbers in the left bottom of each reconstruction indicate the NMSE within ROI. The display window is 280mm X 280mm.

This article has been accepted for publication in a future issue of this journal, but has not been fully edited. Content may change prior to final publication. Citation information: DOI 10.1109/TCI.2019.2922477, IEEE Transactions on Computational Imaging

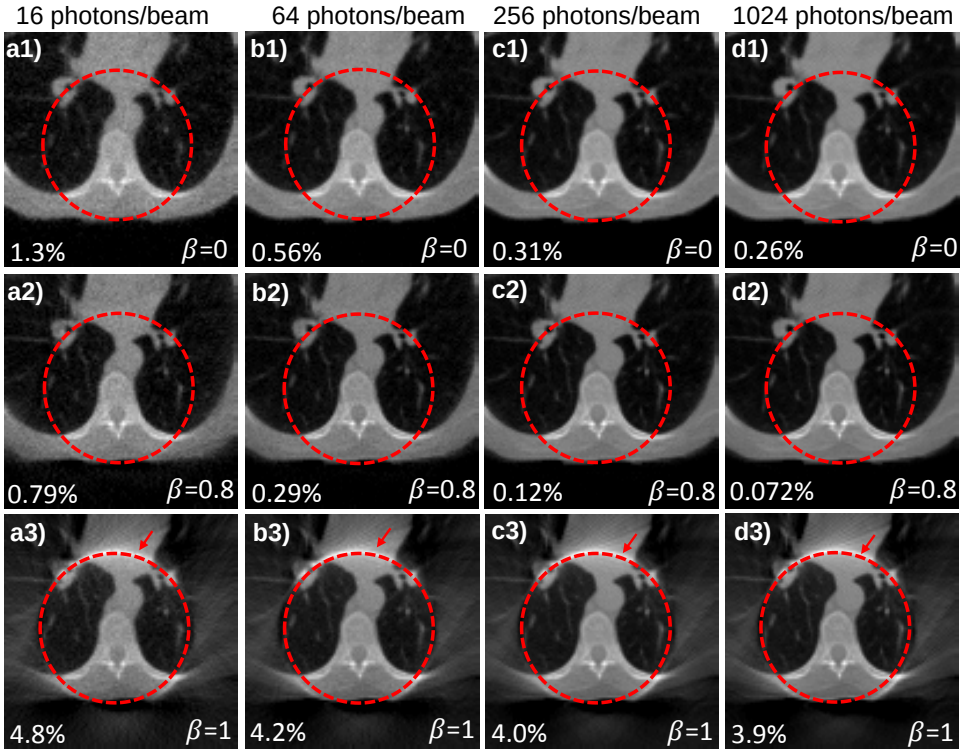

Fig. 8: Reconstruction of the abdomen phantom with different total photon budget (a) 16, (b) 64, (c) 256 and (d) 1024 photons per beam on average for (1) β=0 (uniform distribution), (2) optimized β, and (3) β=1, with γ=16. The ROI is marked by the red circle. The red arrows highlight the truncation artifacts. The numbers in the left bottom of each reconstruction indicate the NMSE within ROI. The display window is 200mm X 200mm.

B. Phantom simulation with total-variation (TV) prior

In this section, we demonstrate the photon allocation strategies applied to ROI reconstruction with TV prior. The object in this simulation is a piecewise-constant Shepp-Logan phantom (Fig. 9(a)). Fig. 9 (b) plots the NMSE of the ROI reconstruction with different (β,γ) combinations compared with the ground truth. Fig. 9 (c, d) shows the photon map and ROI reconstruction at the optimal and interior measurement strategies. The best reconstruction performance was attained at β=0.9, γ=16, with an NMSE of 0.40%±0.04%. The optimal regularization parameter τ is $10^{1.5}$. In contrast, the reconstruction from interior strategy (β=1, γ=16) has an NMSE of 15%±5%, which was obtained at the optimal τ=$10^{5.5}$. We speculate that the smooth and low-contrast ROI reconstruction in Fig. 9 (c2) is mainly due to the large regularization parameter required for lowering the reconstruction variance in ROI. Allocating 10% of the photon budget to the exterior region obviates the need for a strong piecewise constant regularizer, thus achieving superior reconstruction quality than TV-based interior reconstruction.

C. Resolution target imaging

Based on the high consistency between the analytical model and the numerical estimator, we were able to approximately predict the optimized photon-allocation strategy for an experimental object with L2 prior. Fig. 10 shows a full-scan CT image of an acrylic resolution target acquired with 1s integration time and an average photon count of 589 per pencil beam, which was used as the reference. The ROI reconstruction was performed at various photon allocation strategies with 16 photons per beam on average. For each strategy, we calculated the bias and variance with 6 regularization parameters τ ranging from 10^1~$10^{3.5}$, and selected the one giving minimal predicted MSE for use in the SPIRAL reconstruction. Fig. 10 plots the analytically-predicted reconstruction MSE (compared to the reference in (a)) inside the ROI as a function of interior/exterior ratio β and the shape parameter γ. From our prediction, the smallest ROI reconstruction error was attained at β=0.7, γ=4 with the regularization parameter τ=10^2. Fig. 10 (d, e) shows the measured time intervals **g** (d1-d3) and reconstructions (e1-e3) from 3 photon allocation maps **r** (c1-c3), corresponding to uniform (c1), optimized (c2) and interior (c3) strategies, respectively. The optimized strategy had a reconstruction NMSE of 2.8% at ~30 times reduced photon budget compared to the reference image.

V. Discussions

A. Approximations on the distribution of $\hat{t}$

In Section III.C, we approximated the distribution of the measured CT line integral $\hat{\mathbf{t}}$ with a Gaussian distribution. Fig. 11 compares the distribution $q_j(\hat{t}_j|t_j;r_j)$ (Eq. (9)), the first-order simplification (Eq. (10)) and our Gaussian approximation (Eq. (11) without remainder $R(\hat{t}_j)$) for r_j ranging from 1 to 32, and t_j=1.0. The difference between $q_j(\hat{t}_j|t_j;r_j)$ and the first-order simplification is

This article has been accepted for publication in a future issue of this journal, but has not been fully edited. Content may change prior to final publication. Citation information: DOI 10.1109/TCI.2019.2922477, IEEE Transactions on Computational Imaging

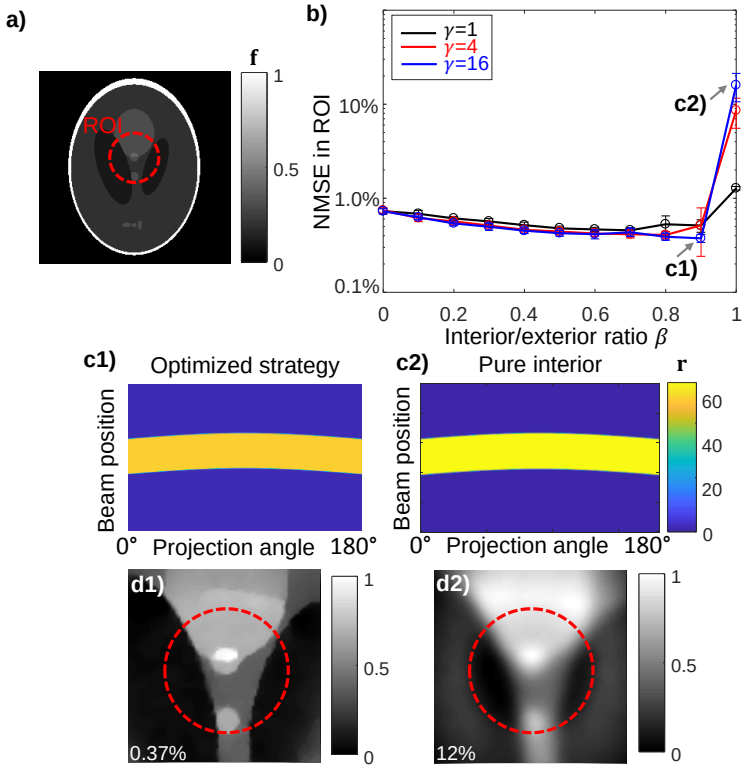

Fig. 9: Photon allocation strategy for TV prior. (a) Shepp-Logan phantom and ROI in the simulation. (b) NMSE in ROI vs. interior/exterior ratio β for γ=1, 4, and 16. (c) Photon allocation map for (c1) optimized strategy (β=0.9, γ=16) and (c2) conventional truncated projection (β=1, γ=16). (d1, d2) Reconstruction from (c1), (c2), respectively. The ROI is highlighted in (d1, d2). The numbers in the left bottom of each reconstruction indicate the NMSE within ROI.

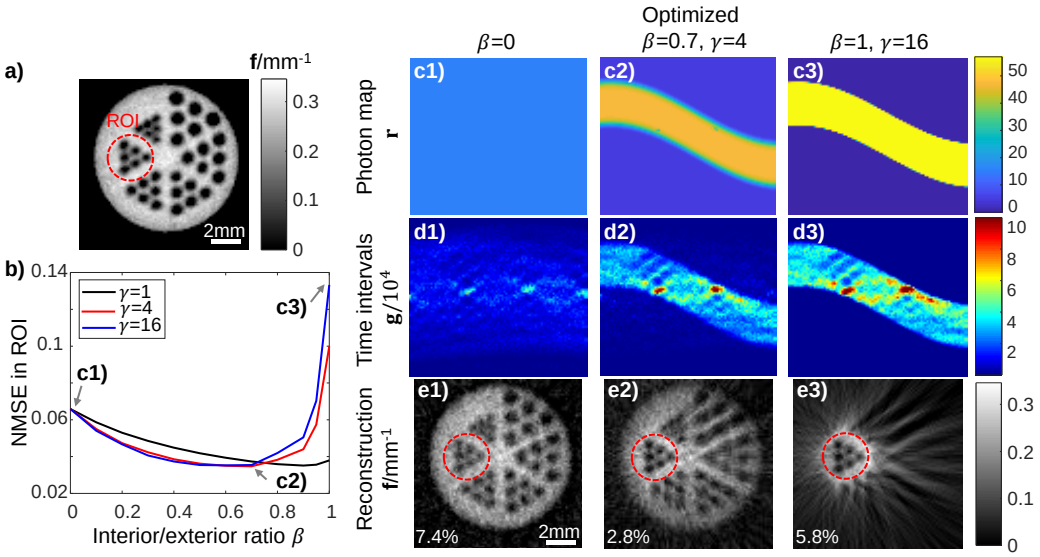

Fig. 10: Comparison between different photon allocation strategies for the resolution target. (a) Full-scan CT image of the resolution target. The ROI covers the 0.6mm line-width group. (b) Predicted reconstruction MSE in ROI with respect to different photon allocation strategies, expressed in terms of the interior/exterior ratio β and the shape parameter γ. (c–e) Examples of the photon allocation strategies, experimental measurements and the corresponding ROI reconstructions from (1) uniform photon counts (2) optimized photon allocation map (3) interior measurement with β=1, γ=16. The average photon count was 16 per beam. All scale bars represent 2mm. The ROI is marked by the red, dashed circle in (a) and (e). The numbers in the left bottom of each reconstruction indicate the MSE within ROI.

negligible. The discrepancy mainly arises from the remainder term $R(\hat{t}_j)$ in Eq. (11), which introduces negative skew on the normal distribution and lowers the mean of $\hat{t}_j$. Fig. 11 (e) quantifies the bias, variance and MSE of the distribution $q_j(\hat{t}_j|t_j;r_j)$ with respect to the ground truth t_j. The variance and MSE of the unbiased Gaussian approximation, $1/r_j$, is also plotted for comparison. As the photon number increases to 16 and above, the bias contributes to less than 1% in the MSE,

This article has been accepted for publication in a future issue of this journal, but has not been fully edited. Content may change prior to final publication. Citation information: DOI 10.1109/TCI.2019.2922477, IEEE Transactions on Computational Imaging

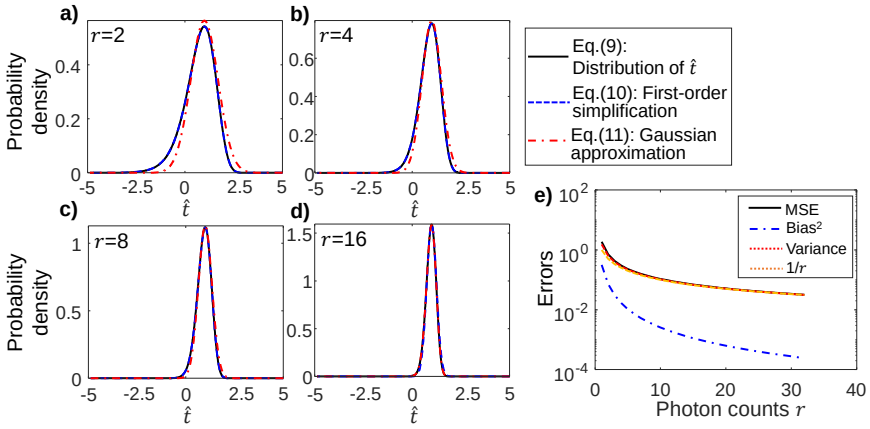

Fig. 11: Comparison between the distribution of $\hat{t}$ and our approximations. (a-d) Original distribution of $\hat{t}$, first-order simplification and Gaussian approximation for r=2, 4, 8 and 16, t=1.0. (e) Bias^2, variance and MSE of $\hat{t}$ with respect to the ground truth t. The dashed, orange curve plots the variance of Gaussian-approximated, unbiased distribution of $\hat{t}$ (Eq. (11)).

which indicates that the unbiased normal distribution is a good approximation to $q_j(\hat{t}_j|t_j;r_j)$. Notice that for a different ground truth t_j, Eq. (10) implies that the peak of the distributions in Fig. 11 (a-d) would shift, while their shapes remain the same.

B. *Approximations on the MAP objective function*

In our analytical models and numerical simulations, the regularization parameter was selected by minimizing the reconstruction MSE. Fig. 12 (a) plots the bias, variance and MSE of both the negative binomial (Eq. (6)) and the approximated (Eq. (15)) estimators with respect to different regularization levels τ. Here we chose the optimized photon allocation strategy (β=0.8, γ=16) of the abdomen phantom as an example. All plotted values are normalized with respect to the L2-norm of the object ground truth in ROI. The bias-variance trade-off in the MSE of the estimator can be clearly seen in both analytical and modified SPIRAL estimator. Both curves predict a choice of τ=10^2 to minimize the reconstruction MSE. It is clear from Fig. 12 (a) that Eq. (15) differs from the numerical estimator in terms of variance at small regularization parameters τ, and bias at large τ. The over-estimation of variance is caused by the absence of non-negativity constraint, which removes the negative portion in the distribution of the numerical estimator and thus reduces its variance. The discrepancy in bias is caused by approximating the shape of log-likelihood function $l(\mathbf{f}|\mathbf{g};\mathbf{r})$ with a quadratic function. This error becomes especially prominent as the solution moves away from the center of the quadratic function at high τ.

Fig. 12 (b-c) details the pixel-wise bias square, variance and MSE map from the analytical approximation and modified SPIRAL estimator at τ=10^2. Due to the higher photon count, the variance within ROI is smaller than the exterior region in both (b2) and (c2). The variance map of (c2) shows object-dependent features that do not exist in the analytical approximation (Eq. (20)). This is because the modified SPIRAL estimator with positivity constraint (Eq. (6)) is a non-linear function of $\hat{\mathbf{t}}$. Table 4 summarizes the NMSE within the ROI and whole sample. Despite the discrepancy in the

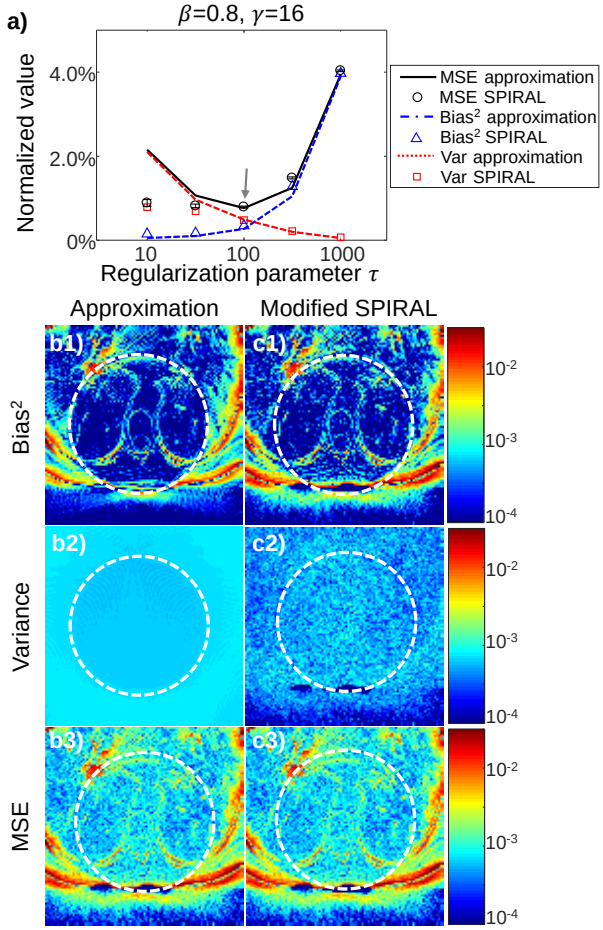

Fig.12: Comparison between the approximated and SPIRAL estimator in terms of bias, variance and MSE map, normalized by the L2-norm of ROI ground truth. (a) Bias square, variance and MSE within the ROI as a function of the regularization parameter τ for the photon map β=0.8, γ=16. (b-c) Bias^2 (b1,c1), variance (b2,c2) and MSE (b3,c3) map of the object from (b) analytical approximation, (c) SPIRAL with negative binomial objective function. The white, dashed circles mark the ROI. The display window is 200mm X 200mm.

variance maps between modified SPIRAL and our approximation, for τ on the order of ~10^2, which we pick in the reconstruction, the NMSE of the numerical simulation matches well with Eq. (21) within the ROI.

This article has been accepted for publication in a future issue of this journal, but has not been fully edited. Content may change prior to final publication. Citation information: DOI 10.1109/TCI.2019.2922477, IEEE Transactions on Computational Imaging

TABLE 4:
COMPARISON OF NMSE BETWEEN THE ANALYTICAL APPROXIMATION AND MODIFIED SPIRAL WITH NEGATIVE BINOMIAL LIKELIHOOD

NMSE	Analytical approximation	Modified SPIRAL
Within ROI	0.76%	0.79%
Whole phantom	3.8%	4.5%

C. *Truncation artifacts in ROI reconstruction*

The truncation artifacts of interior tomography are mainly concentrated near the edge of ROI [33,34], and by extending the truncated sinogram beyond ROI boundary with a circular or Gaussian profile, the truncation error can be effectively reduced. From the photon allocation standpoint, by simply extending the conventional truncated projection slightly larger than the ROI, it might be possible to "exclude" the artifact region. This strategy can be implemented by further generalization of the parameterized photon allocation function in Eq. (22) to allow a non-linear roll-off from the interior to the exterior region. Here we perform an analysis on the extended truncation approach (β=1, γ=16) by shrinking the weight matrix $\mathbf{w}$ in Eq. (21) from whole ROI to a reduced ROI with 10 pixels smaller in diameter, the weight matrix of which is denoted as $\mathbf{w}_p$. Table 5 shows the result of the NMSE for the extended truncation approach. We can see that though the NMSE of this approach has reduced the truncation error (c.f. Table 3), the optimized allocation strategy still outperforms this extended truncation approach by more than 3 times, and uniform strategy by 2~4 times. Though extended truncation avoids the artifacts near the boundary, the reconstruction bias of $\hat{\mathbf{f}}$ persists, contributing to the majority of the reconstruction error, which is consistent with previous results [35].

TABLE 5:
THE NMSE FOR UNIFORM, OPTIMIZED AND INTERIOR PHOTON ALLOCATION STRATEGIES WITHIN PARTIAL ROI

Average photons per beam	16	64	256	1024
Optimal β	0.8	0.9	0.9	0.9
Uniform strategy NMSE	1.1% ±0.04%	0.49% ±0.04%	0.26% ±0.03%	0.24% ±0.01%
Optimal strategy NMSE	0.64% ±0.03%	0.24% ±0.01%	0.10% ±0.003%	0.059% ±0.002%
Interior strategy NMSE	1.95% ±0.03%	1.63% ±0.01%	1.56% ±0.05%	1.52% ±0.05%

VI. CONCLUSION

In summary, we have proposed a few-photon measurement framework and its corresponding statistical reconstruction algorithm optimized for region-of-interest x-ray computed tomography. The demonstrated framework is capable of reconstructing an ROI with an average detected photon budget of 16 photons per beam. We model the numerical reconstruction as a Bayesian estimator, and study its bias, variance and MSE with various levels of regularization. The analytical model with L2 prior consistently agrees with the simulation, and correctly predicts the trend of MSE for different photon allocation maps. Although predicting MSE involves the ground truth of the attenuation map $\mathbf{f}$, this information can be obtained from a fast, pre-diagnostic scan, which has already been practiced in a number of multi-resolution, region-of-interest CT systems [13,23,36].

The combination of negative binomial photon statistics with an optimized photon allocation strategy presents a novel approach to efficiently utilizing the available photon budget, which is especially attractive for low-photon scenarios. By optimizing the two parameters controlling the profile of the photon allocation, we have demonstrated a ~2-fold improvement in ROI reconstruction compared with uniformly allocating the same photon budget throughout the sample, and a 10~15-fold improvement compared with concentrating all available photons in the ROI. In our numerical experiments, we have discovered that the optimal photon ratio between ROI and exterior region is primarily determined by the ROI diameter relative to the whole object size. A smaller ROI requires more photons outside ROI to lower the NMSE contributed from the noisy exterior region. In a real CT experiment, we were able to faithfully reconstruct an ROI of the resolution target at ~30 times reduced total photon budget.

The proposed time-stamp photon-counting interior tomography scheme can be extended beyond the demonstrated pencil-beam system. To achieve the parallelization of the latest generation CT, we can use a photon-counting detector array and a programmable mask that blocks the individual beam when a predefined photon count is received on each pixel. The energy discrimination capability of the PCDs also allows simultaneous acquisition of attenuation maps in different x-ray energy channels for spectral CT. Finally, the high photon-efficiency associated with the x-ray PCDs could extend our model to the reconstruction of x-ray diffraction tomography [37], where the diffraction signal is intrinsically ~2 orders of magnitude lower than the transmission signal. We envision that our photon-counting tomography framework could be applied to photon-starved environments for both x-ray and visible imaging systems.

ACKNOWLEDGMENT

The authors would like to thank Dr. Alexander Katsevich (Department of Mathematics, University of Central Florida) for helpful discussions.

REFERENCES

[1] D. J. Brenner and E. J. Hall, "Computed Tomography — An Increasing Source of Radiation Exposure," *N. Engl. J. Med.*, vol. 357, no. 22, pp. 2277–2284, Nov. 2007.

[2] D. J. Brenner and C. D. Elliston, "Estimated Radiation Risks Potentially Associated with Full-Body CT Screening," *Radiology*, vol. 232, no. 3, pp. 735–738, Sep. 2004.

[3] S. Kappler *et al.*, "First results from a hybrid prototype CT scanner for exploring benefits of quantum-

counting in clinical CT," in *Proc. SPIE 8313, Medical Imaging 2012: Physics of Medical Imaging*, 2012, no. March 2012, p. 83130X.

[4] K. Taguchi and J. S. Iwanczyk, "Vision 20/20: Single photon counting x-ray detectors in medical imaging," *Med. Phys.*, vol. 40, no. 10, p. 100901, 2013.

[5] E. N. Gimenez *et al.*, "Characterization of Medipix3 With Synchrotron Radiation," *IEEE Trans. Nucl. Sci.*, vol. 58, no. 1, pp. 323–332, 2011.

[6] W. A. Kalender *et al.*, "Technical feasibility proof for high-resolution low-dose photon-counting CT of the breast," *Eur. Radiol.*, vol. 27, no. 3, pp. 1081–1086, 2017.

[7] P. M. Shikhaliev, T. Xu, and S. Molloi, "Photon counting computed tomography: Concept and initial results," *Med. Phys.*, vol. 32, no. 2, pp. 427–436, 2005.

[8] M. Beister, D. Kolditz, and W. A. Kalender, "Iterative reconstruction methods in X-ray CT," *Phys. Medica*, vol. 28, no. 2, pp. 94–108, 2012.

[9] A. Markman and B. Javidi, "Integrated circuit authentication using photon-limited x-ray microscopy," *Opt. Lett.*, vol. 41, no. 14, p. 3297, 2016.

[10] T. Hebert and R. Leahy, "A Generalized EM Algorithm for 3-D Bayesian Reconstruction from Poisson Data Using Gibbs Priors," *IEEE Trans. Med. Imaging*, vol. 8, no. 2, pp. 194–202, 1989.

[11] Q. Xu, X. Mou, G. Wang, J. Sieren, E. A. Hoffman, and H. Yu, "Statistical Interior Tomography," *IEEE Trans. Med. Imaging*, vol. 30, no. 5, pp. 1116–1128, May 2011.

[12] D. Shin, A. Kirmani, V. K. Goyal, and J. H. Shapiro, "Photon-Efficient Computational 3-D and Reflectivity Imaging With Single-Photon Detectors," *IEEE Trans. Comput. Imaging*, vol. 1, no. 2, pp. 112–125, Jun. 2015.

[13] D. Kolditz, Y. Kyriakou, and W. A. Kalender, "Volume-of-interest (VOI) imaging in C-arm flat-detector CT for high image quality at reduced dose," *Med. Phys.*, vol. 37, no. 6, pp. 2719–2730, Jun. 2010.

[14] D. Bernard and R. C. Blish, "Considerations for Minimizing Radiation Doses to Components during X-ray Inspection," in *2005 7th Electronic Packaging Technology Conference*, 2005, vol. 2, pp. 697–704.

[15] M. Hadwiger, L. Fritz, C. Rezk-Salama, T. Höllt, G. Geier, and T. Pabel, "Interactive volume exploration for feature detection and quantification in industrial CT data," *IEEE Trans. Vis. Comput. Graph.*, vol. 14, no. 6, pp. 1507–1514, 2008.

[16] G. Wang and H. Yu, "The meaning of interior tomography," *Phys. Med. Biol.*, vol. 58, no. 16, p. R161, 2013.

[17] Y. Ye, H. Yu, Y. Wei, and G. Wang, "A general local reconstruction approach based on a truncated hilbert transform," *Int. J. Biomed. Imaging*, vol. 2007, 2007.

[18] X. Jin, A. Katsevich, H. Yu, G. Wang, L. Li, and Z. Chen, "Interior Tomography With Continuous Singular Value Decomposition," *IEEE Trans. Med. Imaging*, vol. 31, no. 11, pp. 2108–2119, Nov. 2012.

[19] G. Wang and H. Yu, "Compressed sensing based interior tomography," *Phys. Med. Biol.*, vol. 54, no. 9, p. 2791, 2009.

[20] J. Yang, H. Yu, M. Jiang, and G. Wang, "High Order Total Variation Minimization for Interior Tomography.," *Inverse Probl.*, vol. 26, no. 3, pp. 350131–3501329, 2010.

[21] F. Schaff *et al.*, "Correlation of X-ray vector radiography to bone micro-architecture.," *Sci. Rep.*, vol. 4, p. 3695, 2014.

[22] M. N. Lakshmanan *et al.*, "An X-ray scatter system for material identification in cluttered objects: A Monte Carlo simulation study," *Nucl. Instruments Methods Phys. Res. Sect. B Beam Interact. with Mater. Atoms*, vol. 335, pp. 31–38, 2014.

[23] G. Tisson, P. Scheunders, and D. Van Dyck, "3D region of interest x-ray CT for geometric magnification from multiresolution acquisitions," in *2004 2nd IEEE International Symposium on Biomedical Imaging: Macro to Nano (IEEE Cat No. 04EX821)*, 2004, vol. 2, pp. 567–570.

[24] N. Mail, D. J. Moseley, J. H. Siewerdsen, and D. A. Jaffray, "The influence of bowtie filtration on cone-beam CT image quality.," *Med. Phys.*, vol. 36, no. 1, pp. 22–32, Jan. 2009.

[25] Z. Zhu and S. Pang, "Few-photon computed x-ray imaging," *Appl. Phys. Lett.*, vol. 113, no. 23, p. 231109, Dec. 2018.

[26] R. L. Siddon, "Fast calculation of the exact radiological path for a three-dimensional CT array," *Medical Physics*, vol. 12, no. 2. pp. 252–255, 1985.

[27] I. A. Elbakri and J. A. Fessler, "Statistical image reconstruction for polyenergetic X-ray computed tomography.," *IEEE Trans. Med. Imaging*, vol. 21, no. 2, pp. 89–99, Feb. 2002.

[28] D. Zhang and T. Z. Huang, "Generalized Tikhonov regularization method for large-scale linear inverse problems," *J. Comput. Anal. Appl.*, vol. 15, no. 7, pp. 1317–1331, 2013.

[29] G. D. Hugo *et al.*, "Data from 4D Lung Imaging of NSCLC Patients," *Cancer Imaging Arch.*, 2016.

[30] Z. T. Harmany, R. F. Marcia, and R. M. Willett, "This is SPIRAL-TAP: Sparse Poisson Intensity Reconstruction ALgorithms—Theory and Practice," *IEEE Trans. Image Process.*, vol. 21, no. 3, pp. 1084–1096, Mar. 2012.

[31] A. Beck and M. Teboulle, "Fast gradient-based algorithms for constrained total variation image denoising and deblurring problems," *IEEE Trans. Image Process.*, vol. 18, no. 11, pp. 2419–2434, 2009.

[32] F. Natterer, *The Mathematics of Computerized Tomography*, no. iv. Siam, 1986.

[33] J. W. Moore, H. H. Barrett, and L. R. Furenlid, "Adaptive CT for high-resolution, controlled-dose, region-of-interest imaging," *IEEE Nucl. Sci. Symp. Conf. Rec.*, pp. 4154–4157, 2009.

[34] Z. Zhu, R. A. Ellis, and S. Pang, "Coded cone-beam x-ray diffraction tomography with a low-brilliance tabletop source," *Optica*, vol. 5, no. 6, pp. 733–738, 2018.